https://doi.org/10.5194/tc-2020-153
Preprint. Discussion started: 23 June 2020
© Author(s) 2020. CC BY 4.0 License.

The Cryosphere Discussions

Non-normal flow rules affect fracture angles in sea ice viscous-plastic rheologies

Damien Ringeisen[1], L. Bruno Tremblay[2], and Martin Losch[1]

[1]Alfred-Wegener-Institut, Helmholtz-Zentrum für Polar- und Meeresforschung, Bremerhaven, Germany
[2]Department of Atmospheric and Oceanic Sciences, McGill University, Montréal, Canada

Correspondence: Damien Ringeisen (damien.ringeisen@awi.de)

Abstract. The standard viscous-plastic (VP) sea ice model with an elliptical yield curve and normal flow rule does not simulate fracture angles below 30° in uni-axial compression, in stark contrast with observations of Linear Kinematic Features (LKFs) in the Arctic Ocean. In this paper, we remove the normality constraint in the standard VP model and study its impact on the fracture angle in a simple uni-axial compressive loading test. To this end, we introduce a plastic potential independent of the yield curve that defines the post-fracture deformations or flow rule. The numerical experiments show that the fracture angle strongly depends on the flow rule details. For instance, a plastic potential with an ellipse aspect ratio smaller than that of the standard ellipse gives fracture angles that are as low as 22°. A newly adapted theory – based on one developed from observations of granular material – predicts numerical simulations of the fracture angles for plastic materials with a normal or non-normal flow rule with a root-mean-square error below 1.3°. Implementing an elliptical plastic potential in the standard VP sea ice model requires only minor modifications. The modified rheology, however, takes longer to solve numerically for a fixed level of numerical convergence. In conclusion, the use of a plastic potential addresses several issues with the standard VP rheology: the fracture angle can be reduced to values within the range of satellite observations and it can be decoupled from the exact shape of the yield curve. Furthermore, a different plastic potential function will be required to change the post-fracture deformation along the fracture lines (convergence or divergence) and to make the fracture angle independent on the confining pressure (as in observations).

1 Introduction

Sea ice plays a significant role in the energy budget of the climate system and therefore has a strong influence on future climate projections. Linear Kinematic Features (LKFs), narrow lines of deformation observed in the Arctic sea ice cover, emerge in high-resolution simulations (Kwok, 2001; Hutchings et al., 2005). LKFs in the Arctic sea ice cover influence the Earth system in many ways: heat and matter exchange take place primarily over open water (Badgley, 1965). Salt rejection during ice formation in leads creates dense water and influences the thermohaline circulation (Nguyen et al., 2011, 2012; Itkin et al.,

https://doi.org/10.5194/tc-2020-153
Preprint. Discussion started: 23 June 2020
© Author(s) 2020. CC BY 4.0 License.

The Cryosphere Discussions
Open Access
EGU

2015). The ice strength locally depends on the ice thickness, which in turn is affected by sea ice fracture with thermodynamical growth in opening leads and with local dynamical growth during ridge formation.

In granular media like sea ice (Overland et al., 1998), deformation is localized along pairs of LKFs (Anderson, 1942; Erlingsson, 1988). Note, that in this study, we consider sea ice to be granular not only in the marginal ice zone, but also in pack ice, where ice floes are densely packed. The intersection angles between the LKFs influence the deformation field; thus, the local sea ice strength and the emergent sea ice anisotropy (Aksenov and Hibler, 2001). This anisotropy then influences future deformation and fracture line orientation, which will have impacts on the local sea ice mass balance. Therefore, reproducing the LKFs patterns, density, and orientation is important for accurate sea ice and climate projections at high-resolution.

LKFs have been studied for several decades using observations (Stern et al., 1995; Kwok, 2001; Schulson and Hibler, 2004; Weiss et al., 2007) and numerical models (Spreen et al., 2017; Hutter et al., 2018). In viscous-plastic (VP) sea ice models, LKFs are created because the ice is modeled as a highly viscous material between narrow zones of plastic deformation (Hutchings et al., 2005). This behaviour has been argued to be the reason why temporal intermittency and spatial localization are low in VP models, leading to a spatial and temporal scaling of LKFs that is different from observations (Rampal et al., 2016). New models have been designed to represent sea ice fracture, for example, brittle models with a damage parameter that keeps the memory of previous fracture (Rampal et al., 2016; Dansereau et al., 2016), or anisotropic viscous-plastic rheologies models (Wilchinsky and Feltham, 2006; Heorton et al., 2018). Still, as of today, the viscous-plastic rheology with elliptical yield curve and normal flow rule (Hibler, 1979) is the *de facto* standard rheology. For example, of the 33 Global Climate Models from the Climate Model Inter-comparison Project 5 (CMIP5), 30 use the standard VP rheology with an elliptical yield curve and normal flow rule (Stroeve et al., 2014).

Some of the criticised issues of the standard VP rheology have been addressed. For example, high-resolution VP models also reproduce observed intermittency and spatial localization, even without brittle fracture dynamics; and the origin of intermittency remains an open question (Bouchat and Tremblay, 2017; Hutter et al., 2018; Bouchat et al., 2020, submitted manuscript). However, the distribution of intersection angles between LKFs in the Radarsat Geophysical Processor System (RGPS) dataset and the standard sea ice VP model with an elliptical yield curve with ellipse ratio $e = 2$ (Hibler, 1979) dot not agree (Hutter et al., 2019).

The orientation of LKFs has been the subject of many studies in the field of engineering and granular materials (called shear bands in this field). Two classical solutions coexist and set two limit angles for the orientation of fractures: the Coulomb angle (static behaviour) and the Roscoe angle (dynamic behaviour). The Coulomb angle of fracture θ_C between the fracture line and the first principal stress is determined from the Mohr-Coulomb criterion. It is a function only of the internal angle of friction ϕ (Coulomb, 1773; Mohr, 1900):

$$\theta_C = \frac{\pi}{4} - \frac{\phi}{2}. \tag{1}$$

Roscoe (1970) challenged the coulombic theory by considering the case of dilatant material and found from experiments with sand that the dilatancy angle δ is the main parameter determining the orientation of shear bands (see Fig. 6 in Tremblay and

https://doi.org/10.5194/tc-2020-153
Preprint. Discussion started: 23 June 2020
© Author(s) 2020. CC BY 4.0 License.


Mysak, 1997, for a definition of the dilantancy angle δ in the context of sea ice modeling.). The Roscoe angle of fracture is

$$\theta_R = \frac{\pi}{4} - \frac{\delta}{2}. \tag{2}$$

A general theory derived from experiments with sand that takes into account both the angle of friction and the angle of dilation combines the Coulomb and Roscoe angles as (Arthur et al., 1977; Vardoulakis, 1980):

$$\theta_A = \frac{\pi}{4} - \frac{1}{4}(\phi + \delta). \tag{3}$$

Tremblay and Mysak (1997) used this general theory to design their sea ice rheology. Vermeer (1990) proposed a theoretical framework based the grain size and showed that the angle of fracture in most experiments lie between the two extremes: $\theta_C \leq \theta \leq \theta_R$, with $\delta < \phi$ in granular materials like sand. If $\phi = \delta$ then $\theta_R = \theta_C = \theta_A$, and the flow rule is normal to the yield curve. In other words, the principal axes of stress and the principal axes of strain are coaxial. This condition, however, is not generally satisfied for granular materials (Balendran and Nemat-Nasser, 1993). Experiments with sand have shown differences between ϕ and δ of the order of 30° (Vardoulakis and Graf, 1985; Bolton, 1986). Note that both mechanisms, friction and dilatancy, are not radically different: a larger dilatancy angle implies a larger grain size, more contact normals, hence more friction. Ringeisen et al. (2019) used the theory of the internal angle of friction with a normal flow rule in their appendix B to link fracture angles to rheology.

The fracture angles with the standard sea ice rheology cannot be smaller than 30° in uni-axial compression, even by changing the ellipse aspect ratio e (Ringeisen et al., 2019). This minimum angle is in conflict with observations that report fracture angles (half of the intersection angles) generally below 30°. Observations report fracture angles of $14°$ (Marko and Thomson, 1977), $15 \pm 1.5°$ (Erlingsson, 1988), 17° to 18° (Cunningham et al., 1994), $24°$ ($\mu = 0.9$, Weiss and Schulson, 2009), and 20° to 25° (Hutter and Losch, 2020). Further, uni-axial compression experiments (Ringeisen et al., 2019) showed that: (1) the angle of fracture is a function of the gradient of shear strength to compressive strength set by the ellipse aspect ratio, (2) the ellipse aspect ratio determines the divergence along the LKFs, and (3) the fracture angle is a function of the confining pressure. These three properties of the standard VP rheology do not comply with the theory and observations of granular media behaviour, namely that shear band orientations and divergent/convergent motion at the slip lines are a function solely of the shear strength of the material and orientation of the contact normals (or dilatation angle). This unphysical behaviour of the standard VP rheology is connected to the shape of the yield curve in conjunction with a normal flow rule.

The flow rule has the advantage that it can be observed with remote sensing methods, contrary to stress which need in-situ measurements. The ratio of shear and divergence along the LKFs allows to infer the dilatancy angle. Observations show that most of the deformation takes place in shear, with 98% of deformations showing more shear than divergence or convergence (Stern et al., 1995). The ellipse ratio of the standard model can be modified to fit this distribution (Bouchat and Tremblay, 2017). Also, laboratory experiments with first-year ice showed that flow rules are non-normal during brittle failures (Weiss et al., 2007). Separating the link between the fracture angle and the flow rule from the yield curve is necessary to design rheologies that are consistent with observed sea ice deformation.

This paper focuses on VP rheologies. Different models represent sea ice dynamics with different material properties, for example, Viscous-Plastic (VP, Hibler, 1977), Elastic-Plastic (EP, Coon et al., 1974), or Maxwell-Elasto-Brittle (MEB, Dansereau

https://doi.org/10.5194/tc-2020-153
Preprint. Discussion started: 23 June 2020
© Author(s) 2020. CC BY 4.0 License.


et al., 2016). In these different classes of models, various rheologies can be defined. In a VP rheology, a yield curve and plastic potential (flow rule) must be defined. The yield curve defines the stress criteria for the transition from small viscous deformations to large plastic deformations. The plastic potential determines the ensuing post-fracture deformation, called the flow rule. The flow rule is normal to the plastic potential (Drucker and Prager, 1952). The plastic potential can be set independently, or be equal to the yield curve. In the latter case, the flow rule is also perpendicular to the yield curve and is called a normal-flow rule or associated flow rule. Several yield curves have been used in sea ice models, some with a normal flow rule (Hibler, 1979; Zhang and Rothrock, 2005) and some with a non-normal flow rule (Ip et al., 1991; Tremblay and Mysak, 1997; Hibler and Schulson, 2000; Wang, 2007). It is important to note that two models with the same material properties sharing the same yield curve but with different flow rules are two different rheologies.

In this paper, we investigate the effects of a non-normal flow rule on fracture angles and present a generalized framework to use with viscous-plastic material with any flow rules (normal or non-normal). To this end, we introduce a plastic potential independent from yield curve. The new model is tested in simple uni-axial loading experiments where the relationship between fracture angle and flow-rule can be easily identified.

The paper is structured as follows. Section 2 describes the model (2.1), the new rheology (2.2), and a general theory linking the fracture angles and a general flow rule (2.3). The sections 3 and 4 describe the idealized experimental setup and the results. Section 5 discusses these results and their implication on current and future rheologies. Conclusions follow in section 6.

2 Sea ice Model and rheology

2.1 Building the sea ice VP constitutive equations

We consider sea ice as a 2D viscous-plastic material. The ice velocities are calculated from the sea ice momentum equations:

$$\rho h \frac{\partial \boldsymbol{u}}{\partial t} = -\rho h f \boldsymbol{k} \times \boldsymbol{u} + \boldsymbol{\tau}_a + \boldsymbol{\tau}_o - \rho h \nabla \phi(0) + \nabla \cdot \boldsymbol{\sigma}, \tag{4}$$

where ρ is the ice density, h is the grid cell averaged sea ice thickness, $\boldsymbol{u}$ is the ice drift velocity field, f is the Coriolis parameter, $\boldsymbol{k}$ is the vertical unit vector, $\boldsymbol{\tau}_a$ is the surface air stress, $\boldsymbol{\tau}_o$ is the ocean drag, $\nabla\phi(0)$ is acceleration from the gradient of sea surface height, and $\boldsymbol{\sigma}$ is the vertically integrated internal ice stress tensor defined by the sea ice VP constitutive equations. The constitutive equations link the stress tensor $\boldsymbol{\sigma}$ to the deformation tensor $\dot{\boldsymbol{\epsilon}}$ and the state variables χ (ice thickness, ice strength, ice concentration, etc.). The components of the strain rate tensor are computed from the velocities as $\dot{\epsilon}_{ij} = \frac{\partial u_i}{\partial x_j}$. The constitutive equations then have the form:

$$\boldsymbol{\sigma} = f(\dot{\boldsymbol{\epsilon}}, \chi). \tag{5}$$

In an ideal plastic model, the stresses are independent of the strain rates; in the VP model the stresses are independent of the strain rates for large deformation events (the plastic states with stresses on the yield curve) and they depend on the strain rates for small deformations (the viscous states with stresses inside the yield curve). It is this set of equations that defines the rheology of sea ice and determines the fracture pattern and the opening or closing along the fractures.

https://doi.org/10.5194/tc-2020-153
Preprint. Discussion started: 23 June 2020
© Author(s) 2020. CC BY 4.0 License.

The Cryosphere Discussions
Open Access
EGU

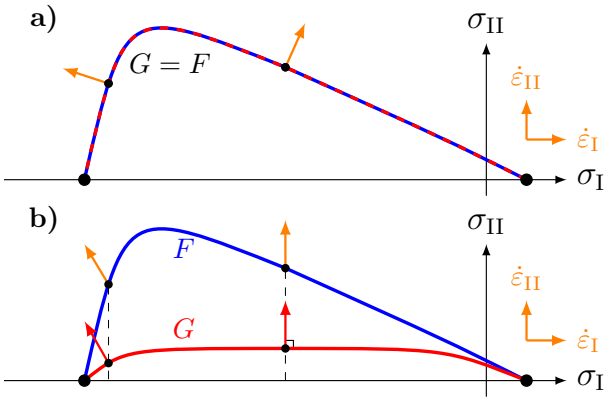

Figure 1. Schematic yield curve F (blue) and plastic potential G (red) for a normal (**a**) and non-normal (**b**) flow rule. The flow rule (orange) for a given stress on the yield curve is normal to the plastic potential (red) for the same σ_I. Note that the stress and strain invariant axes are assumed to coincide.

One of the state variables in the model is the maximal compressive strength P. This variable represents the maximal compressive stress that sea ice can bear in uniform compression before ridging. We use the simple standard relationship (Hibler, 1979):

$$P = P^\star\, h\, e^{-C^\star(1-A)}, \tag{6}$$

where $C^\star$ is a free parameter (typically $C^\star = 20$), h is the mean ice thickness, A is the fractional sea ice area cover in a grid cell, and $P^\star$ is the ice strength of 1 m ice at 100% concentration ($A = 1$). Some other state variables are a function of P; for instance, the tensile strength T is usually defined as $T = k_t \cdot P$, where the tensile factor $k_t > 0$ (König Beatty and Holland, 2010). Others are not, such as the ellipse aspect ratio (Hibler, 1979) or the internal angle of friction (Ip et al., 1991). The equation for the yield curve in a VP model is written in terms of the state variables.

For two-dimensional sea ice, stress is a rank two tensor; thus, it has four components. The yield curve represents the stress states that are deforming plastically while enclosing the states of stress for slow viscous deformations. We express the yield curve as a function of the stresses σ_{ij} and the state variables χ:

$$F(\sigma_{ij}, \chi) = 0. \tag{7}$$

The yield curve can be represented in principal stress (σ_1 and σ_2) or stress invariants space (σ_I and σ_{II}). Figure 1 shows an arbitrary yield curve in stress invariants space. Although equation (7) determines if the deformation is plastic or viscous, it does not determine how the ice will deform after fracture. In order to obtain a closed system of equations, we define a plastic potential that defines the flow rule.

https://doi.org/10.5194/tc-2020-153
Preprint. Discussion started: 23 June 2020
© Author(s) 2020. CC BY 4.0 License.


The plastic potential determines the direction of deformation for stress states on the yield curve. Just as the yield curve, the plastic potential can be written as:

$$G(\sigma_{ij}, \chi) = 0. \tag{8}$$

The direction of the deformation, called the flow rule, is perpendicular to the plastic potential. This is shown in red on Fig. 1b and mathematically expressed by

$$\frac{\partial G}{\partial \sigma_{ij}}(\sigma_{ij}, \chi) = \lambda \dot{\epsilon}_{ij}, \tag{9}$$

where $\lambda > 0$ is the unknown flow rate. The flow rule is applied for stress states on the yield curve at the same compressive stresses (orange arrows in Fig. 1b). If the plastic potential and the yield curve are the same ($G = F$), the flow rule is called an *associative* or *normal* flow rule, as the flow rule is also perpendicular to the yield curve (see Fig. 1a).

Using Eq. (7) and Eq. (9), we can write a system of 5 equations (four from Eq. 9 and one from Eq. 7) for 5 unknowns (σ_{11}, σ_{22}, σ_{12}, σ_{12}, λ). Solving this system of equations allows us to write the constitutive equations for the sea ice model as function of the components of the strain-rate ($\dot{\epsilon}_{11}$, $\dot{\epsilon}_{22}$, $\dot{\epsilon}_{12}$, $\dot{\epsilon}_{21}$) and the state variables χ.

After deriving these constitutive equations, we assume that the stress and strain rate tensors are symmetric, that is, $\sigma_{12} = \sigma_{21}$ and $\dot{\epsilon}_{ij} = \frac{1}{2}\left(\frac{\partial u_i}{\partial x_j} + \frac{\partial u_j}{\partial x_i}\right)$. The symmetry follows from ignoring the rotation in an isotropic medium. Note that we first need to solve this system of equations without using the symmetry condition: the symmetry condition is only invoked at the end. Applying the symmetry before solving the system of equation changes the nature of the initial tensor, and the resulting constitutive equations would be different.

An ideal plastic model, with the stresses independent of the strain rates, has a singularity because the non-linear viscosities tend to infinity as the strain rates tend to zero. Hibler (1977) solved this issue with a regularization that limits the value of the bulk and shear viscosities ζ and η to a maximum value. When the viscosities are capped to their maximum values, the stresses are linearly related to the strain rates and the material behaves as a viscous material.

2.2 Elliptical yield curve with non-normal flow rule

We now build a rheology with an elliptical yield curve and a non-normal flow rule, that is, we use a plastic potential G that is different from the yield curve F. We use a different, but still elliptical plastic potential for simplicity: this choice only requires only minor modifications to a typical VP sea ice model. We define the yield condition F and the plastic potential G as a function of the state variables χ: the ice compression strength P, the ice tensile strength $T = k_t P$ (König Beatty and Holland, 2010), the yield curve's ellipse ratio e_F, and the plastic potential's ellipse ratio e_G by

$$X(\sigma_{\mathrm{I}}, P, e_X, k_t) = \left(\frac{\sigma_{\mathrm{I}} + \frac{P(1-k_t)}{2}}{\frac{P(1+k_t)}{2}}\right)^2 + \left(\frac{\sigma_{\mathrm{II}}}{\frac{P(1+k_t)}{2e_X}}\right)^2 - 1 = 0, \tag{10}$$

for $X = F, G$ for the yield curve or the plastic potential. Using Eq. (10), we write σ_{II} as a function of σ_{I} as:

$$\sigma_{\mathrm{II},X} = \frac{1}{e_X}\sqrt{P^2 k_t - \sigma_{\mathrm{I}}^2 - \sigma_{\mathrm{I}} P(1-k_t))}. \tag{11}$$

https://doi.org/10.5194/tc-2020-153
Preprint. Discussion started: 23 June 2020
© Author(s) 2020. CC BY 4.0 License.

The Cryosphere Discussions
Open Access
EGU

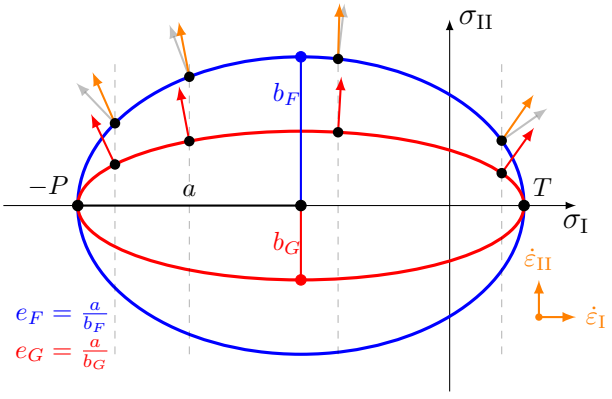

Figure 2. Elliptical yield curve with a non-normal flow rule, a yield curve ellipse aspect ratio $e_F = 2$ (blue) and a plastic potential ellipse aspect ratio $e_G = 4$ (red). The gray and orange arrows show the normal and non-normal flow rules, respectively.

Following Hibler (1977, 1979), we derive the constitutive equations σ_{ij}:

$$\sigma_{ij} = 2\eta\dot{\epsilon}_{ij} + (\zeta - \eta)\,\dot{\epsilon}_{kk}\delta_{ij} - \frac{P(1-k_t)}{2}\delta_{ij}, \tag{12}$$

where the shear and bulk viscosities η and ζ are defined by:

$$\zeta = \frac{P(1+k_t)}{2\Delta} \text{ and } \eta = \frac{\zeta}{e_G^2} = \frac{P(1+k_t)}{2e_G^2\Delta} \tag{13}$$

with

$$\Delta = \sqrt{(\dot{\epsilon}_{11} - \dot{\epsilon}_{22})^2 + \frac{e_F^2}{e_G^4}((\dot{\epsilon}_{11} - \dot{\epsilon}_{22})^2 + 4\dot{\epsilon}_{12}^2)}. \tag{14}$$

Figure 2 shows an example of yield curve and plastic potential, with the resulting flow rule. For $e_G > e_F$, the absolute value of the divergence is smaller and the shear strain rate is larger compared to a normal flow rule ($e_G = e_F$) and vice versa for $e_G < e_F$.

2.3 Linking fracture and flow rule

In this section, we generalize the theory linking the rheological model and the fracture angles in simple uni-axial compressive test (Ringeisen et al., 2019) to materials with a non-associated flow rule. To this end, we follow the theory of Roscoe (1970) where the angle of fracture depends uniquely on the angle of dilatancy of a granular material.

Figure 3 illustrates the case of an arbitrary yield curve with an arbitrary plastic potential. The figure shows the geometrical construction that links the angle of dilatancy δ to the slope of the plastic potential $\tan(\gamma_G)$:

$$\sin(\delta) = \tan(\gamma_G) = -\frac{\partial\sigma_{\mathrm{II},G}}{\partial\sigma_I}. \tag{15}$$

https://doi.org/10.5194/tc-2020-153
Preprint. Discussion started: 23 June 2020
© Author(s) 2020. CC BY 4.0 License.

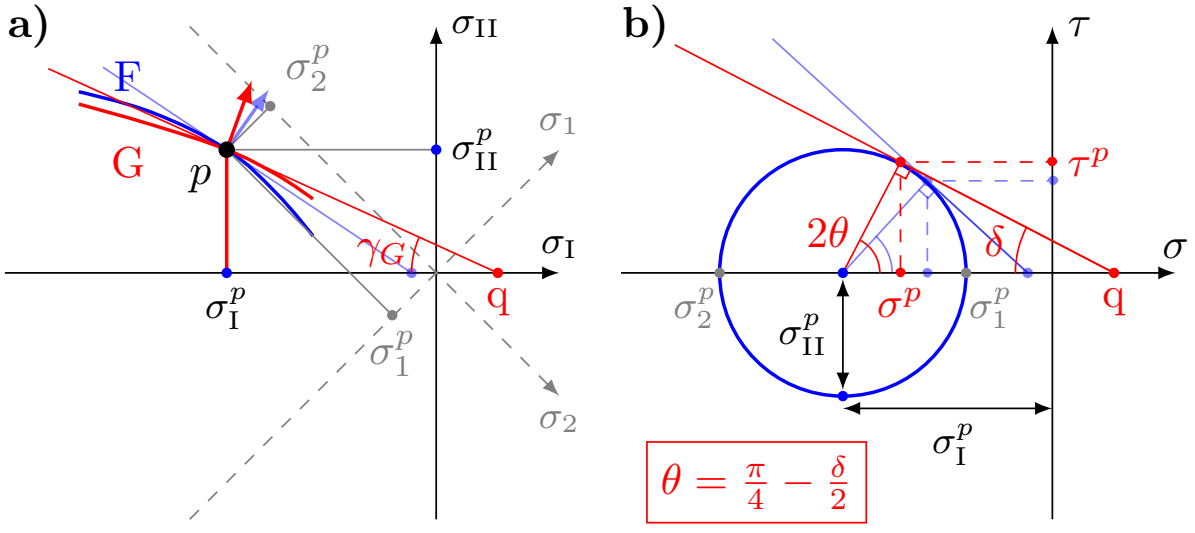

Figure 3. Link between fracture angle and yield curve: **a)** Arbitrary yield curve F (blue) and plastic potential G (red) in stress invariants space. The plastic potential and yield curve intersect at a stress state p for illustration purposes only. The orange arrow is perpendicular to G, but non-normal to the yield curve F. The tangent to the plastic potential G at point p has a slope $\mu_G = \tan(\gamma_G)$ and intersects the σ_{I}-axis at point q (thin red line). For reference, the normal and tangent to the yield curve F are shown as a thin blue arrow and line. Mohr's circle of stress for this stress state (blue) has a radius of σ_{II}^p an centers on σ_{I}^p on the σ_{I} axis. Gray dashed lines show the principal stress axes. **b)** Mohr's circle for the fracture state p in **a)** in the fracture plane of reference (σ, τ) of center σ_{I}^p and radius σ_{II}^p. The thin red line is the tangent to the Mohr's circle that passes through the point q on the σ axis. By this geometrical construction, $\sin(\delta) = \tan(\gamma_G) = \mu_G$ (for $|\mu_G| \leq 1$). δ is called the dilatancy angle. Again for comparison, the transparent blue lines show the corresponding construction for a normal flow rule from panel **a)**.

Note that the minus sign above was included in the derivative of the yield curve in Eq. (B1) and (B2) of Ringeisen et al. (2019). This equation agrees with the definition of Roscoe (1970) $\sin(\delta) = \frac{\dot{\epsilon}_{\mathrm{I}}}{\dot{\epsilon}_{\mathrm{II}}}$, because the ratio of $\dot{\epsilon}_{\mathrm{I}}$ to $\dot{\epsilon}_{\mathrm{II}}$ is equal to the slope of the plastic potential $-\frac{\partial \sigma_{\mathrm{II},G}}{\partial \sigma_{\mathrm{I}}}$, as the flow rule is perpendicular to the plastic potential. Figure 3 also shows the normal flow rule, which, in agreement with the coulombic theory, would lead to different fracture angles (light blue lines). From Fig. 3, the fracture angle can be written as:

$$\theta = \frac{\pi}{4} - \frac{\delta}{2}. \tag{16}$$

Substituting Eq. (15) in the equation above, the relationship between the fracture angle and the plastic potential becomes

$$\theta(\sigma_{\mathrm{I}}) = \frac{1}{2}\left[\frac{\pi}{2} - \arcsin\left(-\frac{\partial \sigma_{\mathrm{II},G}}{\partial \sigma_{\mathrm{I}}}(\sigma_{\mathrm{I}})\right)\right] = \frac{1}{2}\arccos\left(-\frac{\partial \sigma_{\mathrm{II},G}}{\partial \sigma_{\mathrm{I}}}(\sigma_{\mathrm{I}})\right). \tag{17}$$

https://doi.org/10.5194/tc-2020-153
Preprint. Discussion started: 23 June 2020
© Author(s) 2020. CC BY 4.0 License.


We calculate the fracture angles for the elliptical yield curve with non-normal flow rule in uni-axial compression along the y axis. In this case, $\sigma_{11} = \sigma_{12} = 0$, $\sigma_{22} < 0$, and the principal stresses and stress invariants can be written as:

$$\sigma_1 = \frac{1}{2}\left(\sigma_{11} + \sigma_{22} + \sqrt{(\sigma_{11} - \sigma_{22})^2 + 4\sigma_{12}^2}\right) = 0, \tag{18}$$

$$\sigma_2 = \frac{1}{2}\left(\sigma_{11} + \sigma_{22} - \sqrt{(\sigma_{11} - \sigma_{22})^2 + 4\sigma_{12}^2}\right) = \sigma_{22}. \tag{19}$$

$$\sigma_{\mathrm{I}} = \frac{\sigma_1 + \sigma_2}{2} = \frac{\sigma_{22}}{2} \tag{20}$$

$$\sigma_{\mathrm{II}} = \frac{\sigma_1 - \sigma_2}{2} = -\frac{\sigma_{22}}{2} = -\sigma_{\mathrm{I}}. \tag{21}$$

From Eq. 21, the maximum shear stress $\sigma^p_{\mathrm{II},F}$ in the fracture plane in uni-axial compression can be expressed as

$$\sigma^p_{\mathrm{II},F}(\sigma^p_{\mathrm{I}}) = -\sigma^p_{\mathrm{I}}, \tag{22}$$

where p indicates the stress state at the fracture. Figure 4 shows the stress trajectory in principal stress space for uni-axial compression. It also shows how the flow rule changes for the same stress state when using two different elliptical plastic potentials.

In the following, we use the normalized stress invariants $\sigma'_{\mathrm{I}} = \frac{\sigma_{\mathrm{I}}}{P}$ and $\sigma'_{\mathrm{II}} = \frac{\sigma_{\mathrm{II}}}{P}$ to simplify the notation. The slope of yield curve or the plastic potential depends only on e_F and e_G, but not on P. Substituting Eq. (11), σ'_{I}, and σ'_{II} in Eq. (22), we obtain,

$$\sigma'^p_{\mathrm{II}} = -\sigma'^p_{\mathrm{I}} = \frac{1}{e_F}\sqrt{k_t - \sigma'^p_{\mathrm{I}}(\sigma'^p_{\mathrm{I}} + 1 - k_t)}, \tag{23}$$

and solve the first stress invariant σ^p_{I} on the fracture plane in uni-axial compression

$$\sigma'^p_{\mathrm{I}} = \frac{(k_t - 1) - \sqrt{(1-k_t)^2 + 4k_t(1+e_F^2)}}{2(1+e_F^2)}. \tag{24}$$

The slope of the tangent at σ^p_{I} to the plastic potential is given by the derivative of Eq. (11):

$$\frac{\partial \sigma'_{\mathrm{II},G}}{\partial \sigma'_{\mathrm{I}}}(\sigma'^p_{\mathrm{I}}) = \frac{1}{2e_G}\frac{-2\sigma'^p_{\mathrm{I}} - 1 + k_t}{\sqrt{k_t - \sigma'^p_{\mathrm{I}}(\sigma'^p_{\mathrm{I}} + 1 - k_t)}}. \tag{25}$$

Substituting Eq. (24) into Eq. (25), yields

$$\left.\frac{\partial \sigma'_{\mathrm{II},G}}{\partial \sigma'_{\mathrm{I}}}\right|_{\sigma'^p_{\mathrm{I}}} = \frac{1}{e_G e_F}\left(1 - \frac{(1+e_F^2)}{1 + \sqrt{1 + 4\frac{k_t}{(1-k_t)^2}(1+e_F^2)}}\right). \tag{26}$$

or for zero tensile strength ($k_t = 0$),

$$\left.\frac{\partial \sigma'_{\mathrm{II},G}}{\partial \sigma'_{\mathrm{I}}}\right|_{\sigma'^p_{\mathrm{I}}, k_t = 0} = \frac{1}{2e_F e_G}(1 - e_F^2). \tag{27}$$

https://doi.org/10.5194/tc-2020-153
Preprint. Discussion started: 23 June 2020
© Author(s) 2020. CC BY 4.0 License.

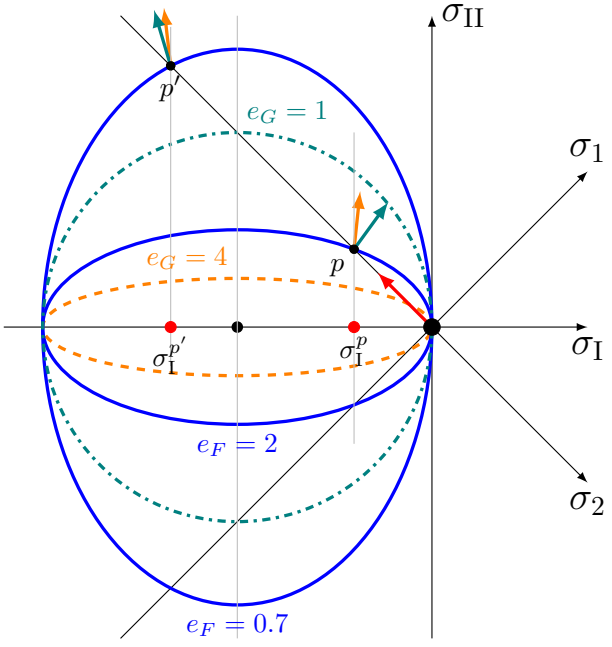

Figure 4. Trajectory of maximum normal stress (red arrow) in a uni-axial loading test experiment in a material with two different elliptical yield curves (blue) and plastic potentials (dashed orange and dash-dotted teal). The orange and teal arrows show the flow rule normal to the plastic potential of the same colour for the same stress state. For $e_G < e_F$, the ratio of divergence to shear increases. The opposite is true for $e_G > e_F$. A similar figure in principal stress space is presented in Ringeisen et al. (2019)

The fracture angle can finally be written as a function of e_G and e_F from Eq. (17):

$$\theta_{e,nn}(e_F, e_G) = \frac{1}{2}\arccos\left(\frac{1}{2e_F e_G}(e_F^2 - 1)\right). \tag{28}$$

As expected, for $e_F = e_G = e$ we recover the fracture angle derived in Ringeisen et al. (2019):

$$\theta_{e,n}(e) = \frac{1}{2}\arccos\left[\frac{1}{2}\left(1 - \frac{1}{e^2}\right)\right]. \tag{29}$$

3 Experimental setup and numerical scheme

Following Ringeisen et al. (2019), we load a rectangular ice floe of 8 km by 25 km with a thickness of $h = 1$ m and a sea ice concentration of $A = 1.0$ (see Fig. 5). The numerical domain has the dimensions $L_x = 10$ km and $L_y = 25$ km. At $y = 0$, we use a closed, solid boundary with a no slip condition (i.e., $u = v = 0$). At $x = 0$ and L_x, we use Neumann boundary conditions:

$$\left.\frac{\partial A}{\partial x}\right|_{x=0,L_x} = \left.\frac{\partial h}{\partial x}\right|_{x=0,L_x} = \left.\frac{\partial u}{\partial x}\right|_{x=0,L_x} = \left.\frac{\partial v}{\partial x}\right|_{x=0,L_x} = 0. \tag{30}$$

https://doi.org/10.5194/tc-2020-153
Preprint. Discussion started: 23 June 2020
© Author(s) 2020. CC BY 4.0 License.

The Cryosphere Discussions
Open Access
EGU

On the left and right sides of the domain ($x < 1\,\mathrm{km}$ and $x > 9\,\mathrm{km}$), we have open water between the ice floe and the boundary to ensure that the boundaries have no effect on the simulation. At ($y = L_y$), we use a Dirichlet boundary condition for ice velocity (v the velocity in y-direction increasing linearly in time simulating an axial loading test) and a Neumann boundary condition for ice thickness and concentration :

$$v(t)|_{y=L_y} = a_v \cdot t \ , \ u(t)|_{y=L_y} = 0 \ ; \ \left.\frac{\partial A}{\partial y}\right|_{y=L_y} = \left.\frac{\partial h}{\partial y}\right|_{y=L_y} = 0 \tag{31}$$

with $a_v = -5 \cdot 10^{-4}\,\mathrm{m\,s^{-2}}$. The grid spacing of the domain is 25 m, and the timestep is 0.1 s.

The non-linear momentum equations are integrated using a Picard solver with 15 000 non-linear (or outer-loop) iterations (Losch et al., 2010). For the linearized problem within each iteration, we use a line successive (over-)relaxation (LSR) method (Zhang and Hibler, 1997), with a tolerance criterion of $|u_k - u_{k-1}|_{\max} < 10^{-11}\,\mathrm{m\,s^{-1}}$, where k is the linear iteration index. We use an inexact approach with only a maximum of 200 linear iterations for the linearized equations; the linearized system does not reach the tolerance criterion for the first non-linear iterations, but does so as the non-linear system approaches a converged solution. We chose a very small tolerance and residual norm for the solution of the linear and non-linear problem in order to simulate a clean fracture with a well defined fracture angle - for comparison with theory and observations. These criteria are much stricter than common recommendations for Arctic sea ice simulations (e.g. Lemieux and Tremblay, 2009). We expect modeling sea ice with a non-normal flow rule to be more challenging than with a normal flow rule. The non-coaxiality of the deviatoric stress and strain rate introduces more complexity because Drucker's postulate for stability is not respected (Vermeer and De Borst, 1984; Balendran and Nemat-Nasser, 1993). This particular uni-axial loading experiment is also complex to solve numerically because the forcing is localized on the boundary, in contrast to real geophysical system integrations where wind and ocean currents are acting over the entire surface of the ice.

The intersection angles between the LKFs are measured with the *Measure Tool* from the GNU Image Manipulation Program (GIMP, version 2.8.16, gimp.org). The first 5 seconds of simulations are used to define the sea ice fracture and calculate the fracture angle. The angle of each fracture lines is measured and used to compute the average fracture angle and the standard deviation $\sigma = \sqrt{\mathrm{VAR}}$. Note that the fracture angles do not depend on resolution, scale, geometry, or boundary conditions (see Ringeisen et al., 2019, their Sec. 3.2). We do not use a replacement pressure scheme (Ip et al., 1991; Ip, 1993), because it has no influence with the angle of fracture (not shown).

4 Results

We study the evolution of the fracture angle θ when the plastic potential changes while the yield curve stays the same (see Fig. 4 for details). In this manner, the ice breaks for the exact same stress state but with a different flow rule. For simplicity, we test here the elliptical yield curve without tensile strength ($k_t = 0$).

Figure 6 shows the fracture pattern for the standard yield curve ellipse ratio $e_F = 2.0$ and three values of the plastic potential ellipse ratio $e_G = 1.4$, 2.0, and 4.0. Following observations and laboratory experiment, the ice fractures have a diamond shape pattern (Erlingsson, 1988; Wilchinsky et al., 2010). With a normal flow rule ($e_G = 2.0$), single pairs of fracture lines with one

https://doi.org/10.5194/tc-2020-153
Preprint. Discussion started: 23 June 2020
© Author(s) 2020. CC BY 4.0 License.

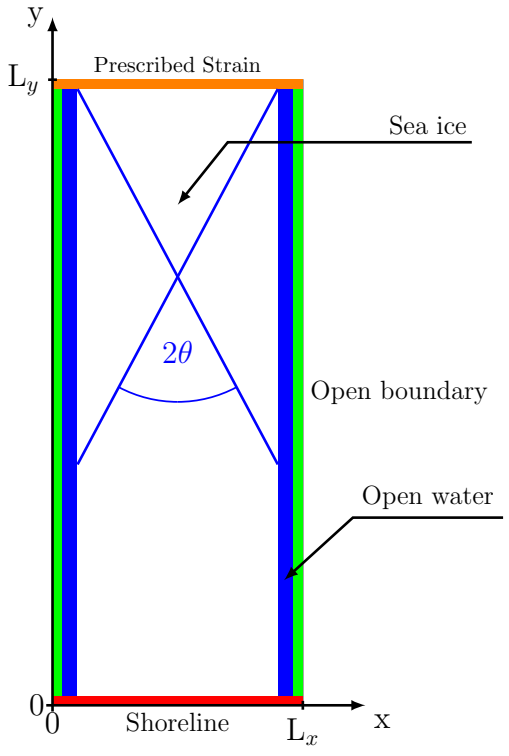

Figure 5. Model domain with a solid wall at $y = 0$ (red), Dirichlet boundary conditions with $\boldsymbol{u} = 0$ at $y = 0$ and prescribed velocities at $y = L_y$. Open boundaries at $x = 0, L_x$ (green) with Neumann boundary conditions. For the conservation of mass, ice thickness and concentration equations (h, A) Neumann boundary conditions are used on all boundaries. θ is the measured fracture angle with respect to the vertical; the blue line represents an LKF.

unique fracture angle, large deformation along the LKFs, and smaller deformations (by several orders of magnitude) within diamond-shape floes are simulated. With the non-normal flow rule ($e_G = 1.4$ and $e_G = 4$) we make three observations:

1. Asymmetric secondary fracture lines appear, in contrast to the normal flow rule simulation. We attribute the asymmetry and presence of secondary fractures to the lack of full numerical convergence associated with the violation of Drucker's principle, or the non-normality of the flow rule (the ratio of divergence to shear strain rate differs from that of the shear to normal stress). For instance, the grid-cell average residual norm (R) decreases by four orders of magnitude for the normal flow rule compared with two orders of magnitude for the non-normal flow rule for the same number of non-linear iterations (15 000); specifically to $R = 8 \times 10^{-4}$ for $e_G = e_F = 2$ to $R = 6 \times 10^{-2}$ for $e_G = 1.4$ and $e_F = 2$. Note that a Jacobian-free Newton-Krylov (JFNK) solver with a quadratic local numerical convergence does not perform better because the global convergence is poor with a combination of localized forcing and high grid resolution (Losch et al., 2014; Williams et al., 2017).

https://doi.org/10.5194/tc-2020-153
Preprint. Discussion started: 23 June 2020
© Author(s) 2020. CC BY 4.0 License.

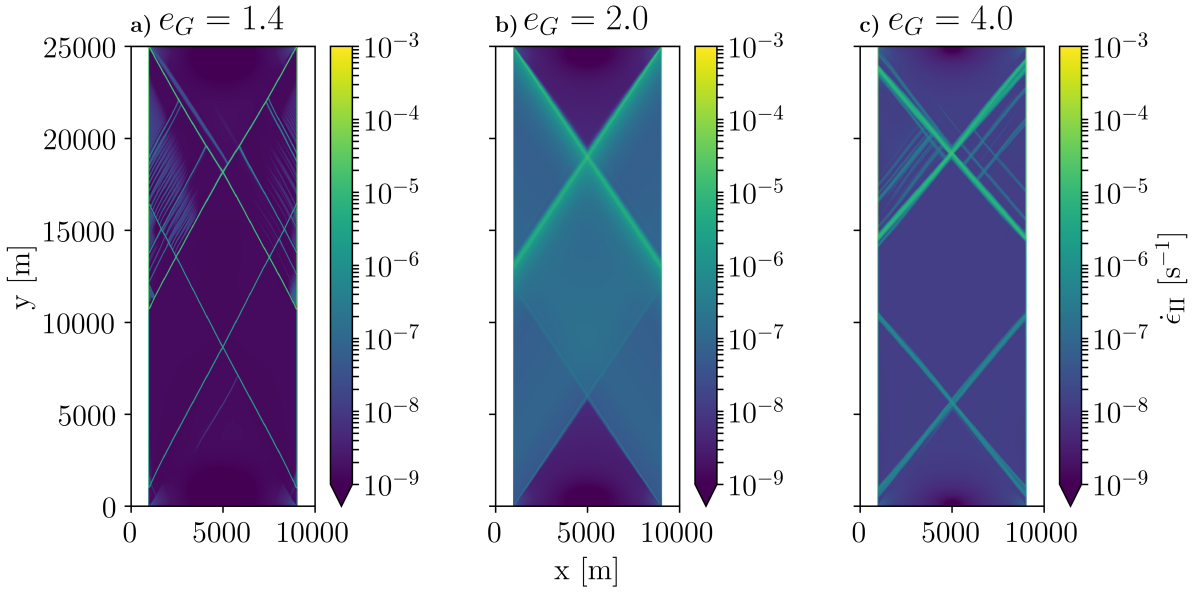

Figure 6. Diamond-shaped fracture pattern for $e_F = 2.0$ and three different values of e_G after five seconds of simulation. For the non-normal flow rule (panels a and c), there are primary and secondary fracture lines, in contrast to the normal flow rule (panel b) where single pair of fracture lines are simulated. The fracture angles are $29.92 \pm 1.28°$ for $e_G = 1.4$, $34.3 \pm 0.25°$ for $e_G = 2.0$, and $40.7 \pm 0.94°$ for $e_G = 4.0$. The error corresponds to two standard deviation (2σ) of the measured fracture angles.

2. The width and activity of the LKFs is also affected by the flow rule. With $e_G = 1.4$, the lines are thinner, the shear along the LKFs is smaller and there is little shear between the fracture lines. With $e_G = 4.0$, the fracture lines are broader, the shear along the LKFs is higher and there is more shear between the fracture lines. With $e_G = 1.4$ the flow rule at the fracture is mainly in divergence, while for $e_G = 4.0$, the flow rule is mainly in shear and there is more stress transmitted to the ice in between the fracture lines.

3. The fracture angle changes as the plastic potential changes. The angles are wider with $e_G = 4$ than $e_G = 1.4$. The effect of flow rule orientation on the fracture angles is discussed below.

We now present results from four sets of simulations with fixed yield curve ellipse ratios at $e_F = 0.7, 1.0, 2.0, 4.0$. For each of these, we test the sensitivity of the results to changes in the plastic potential ellipse ratio e_G. The choice of yield curve ellipse ratios e_F are: the standard value of (Hibler, 1979), values suggested by Bouchat and Tremblay (2017) and Dumont et al. (2009), and an extreme value resulting in a very small shear strength and smaller fracture angles.

Figure 7a shows how the fracture angles evolve as the plastic potential ellipse ratio e_G changes for each of the four values of e_F. There is a clear dependence of the fracture angles on the relative eccentricity of the plastic potential and yield curve. For $e_G > e_F$, the shear strain rate increases along the LKFs and the fracture angle tend toward 45° as e_G increases, in agreement with the theory (Eq. 17). For $e_G < e_F$, the flow rule implies more divergence (for $e_F > 1$, or convergence for $e_F < 1$) and less

https://doi.org/10.5194/tc-2020-153
Preprint. Discussion started: 23 June 2020
© Author(s) 2020. CC BY 4.0 License.

The Cryosphere
Discussions
Open Access
EGU

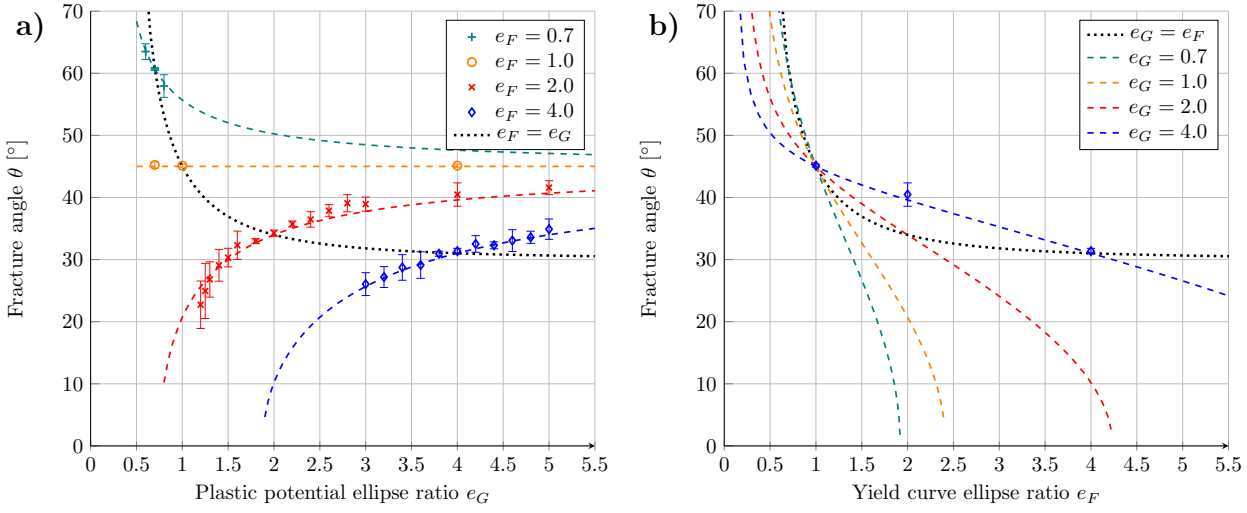

Figure 7. a) Fracture angles as function of the plastic potential ellipse ratio e_G for different yield curve ellipse ratios ($e_F = 0.7$, 1.0, 2.0, and 4.0). The markers with ranges are the mean and variation (2σ) of the fracture angles. The dashed lines show the prediction from the theory (Eq. 28). The R^2 between theory and modeled angles for $e_F = 0.7$, 2.0, and 4.0 are 0.97, 0.95, and 0.97. **b)** Theoretical predictions of the fracture angle as function of e_F with a constant e_G. The black dotted line for the normal flow rule ($e_F = e_G$), is indicated for reference.

shear along the LKFs, and the fracture angles move away from 45° as e_G decreases. More generally, for $e_F < 1$, the fracture angle increases with increasing convergence along the LKFs as e_G decreases. For $e_F > 1$, the fracture angle decreases with increasing divergence as e_G becomes smaller. For $e_F = 1$ (a circular yield curve), the fracture angles are independent of e_G because the fracture takes place at the peak of the yield curve and the flow rule is not affected by changes of the plastic potential ellipse ratio (e_G).

The coloured dashed lines in Fig. 7 show the fracture angles $\theta_{e,nn}(e_F, e_G)$ predicted by Eq. (28). The coefficient of determination R^2 and the root-mean-square error (RMSE) between the simulated angle of fracture and theoretical predictions are 0.974 and 0.37° for $e_F = 0.7$, 0.953 and 1.22° for $e_F = 2.0$, and 0.968 and 0.47° for $e_F = 4.0$. The RMSE is 0.37° for $e_F = 1.0$, R^2 being inapplicable. That is, the theory predicts the fracture angles accurately. This result shows that the flow rule plays a major part in the simulated fracture angle for a given rheology. The black dashed line show the evolution of the fracture angle with a normal flow rule ($e_G = e_F$, Eq. (29)).

For completeness, Figure 7b also show the theoretical predictions for a constant plastic potential ellipse ratio e_G as the yield curve ellipse ratio e_F changes. The modeled angles for $e_G = 4.0$ are shown as an example. The fracture angles become smaller as the e_F increase. Yield curve ellipse ratio smaller than $e_F = 1$ do not create fracture angles below 45°.

https://doi.org/10.5194/tc-2020-153
Preprint. Discussion started: 23 June 2020
© Author(s) 2020. CC BY 4.0 License.


5 Discussion

The idealized experiments using the elliptical yield curve with a non-normal flow rule show that the type of deformation and the fracture angle are intimately linked with the shape of plastic potential. We observe that a yield curve ellipse ratio $e_F < 1$ does not allow for fracture angles smaller than 45° in uni-axial compression when using an elliptical plastic potential, irrespective of the plastic potential elliptical aspect ratio. To reduce the fracture angles with yield curve ellipse ratios $e_F > 1$, one needs to use plastic potential ellipse ratios e_G smaller than the yield curve ellipse ratio, that is, $e_G < e_F$. The numerical experiments show that the use of a plastic potential in a viscous-plastic model allows separating the yield criterion from the resulting deformation (flow rule). This allows to decouple the mechanical strength properties of the material (ice) from its post-fracture behaviour. The results illustrate clearly how the yield curve defines the stress for which the ice will deform, that is, the transition between viscous and plastic deformation, and how the relative shape of the plastic potential with respect to the yield curve defines both the type of deformation (convergence or shear) along the fracture line and the fracture angle. The resulting fracture angles are in excellent agreement with the Roscoe angle predictions (Roscoe, 1970).

Understanding the link between rheology and fracture angle is necessary for choosing or designing a rheology that is capable of reproducing the observed angle of intersection between LKFs and consequently the emerging anisotropy. In principle, it may be possible to solve several inconsistencies of the standard elliptical yield curve with a normal flow rule Ringeisen et al. (discussed in 2019) by using a plastic potential that is independent of the yield curve, namely:

1. In the standard VP model with elliptical yield curve and normal flow rule, adding shear strength increases the fracture angle, contrary to granular matter theory (Coulomb, 1773). This behaviour is linked to the shape of the elliptical yield curve. In principle, we can decrease the fracture angle with increasing shear strength (e_F decreasing) by decreasing e_G, but only if $e_F > 1$. When doing this, the flow rule becomes very non-normal, making the numerical convergence difficult.

2. The angle of fracture in the standard VP model changes with confining pressure unlike laboratory experiments with granular materials (e.g. sand) where the fracture angle is relatively insensitive to the confining pressure (Alshibli and Sture, 2000). This behaviour cannot be eliminated with an elliptical plastic potential, as the normal stresses along the LKFs increases with confining pressure and the flow rule changes from divergence to convergence. A different plastic potential function would change this behaviour. However, this would make the model implementation and numerical convergence more difficult. However, we note that a 3D granular material like sand cannot release stress by ridging as sea ice does. A 2D material, such as sea ice, can ridge and "escape to the 3rd dimension" after fracture.

3. In the standard VP model with a normal flow rule, the divergence and convergence are set by the ellipse ratio of the yield curve, and thus by the relative amounts of compressive and shear stress. The plastic potential ellipse ratio e_G changes the flow rule but does not change the sign of the divergence along the LKFs which is solely determined by the yield curve ellipse ratio e_F. With the elliptical plastic potential, convergent motion remains convergent and only the ratio of shear to

https://doi.org/10.5194/tc-2020-153
Preprint. Discussion started: 23 June 2020
© Author(s) 2020. CC BY 4.0 License.


convergence changes. To change this behaviour, a different shape of plastic potential is required, for example a teardrop plastic potential.

4. The fracture angles in the standard VP models are larger than observed. Using a non-normal flow rule allows us to change the fracture angle in uni-axial compression to values below 30°; something that is not possible with a normal flow rule (Ringeisen et al., 2019).

Other yield curves have been used in previous studies; for instance, the Mohr–Coulomb, the Coulombic yield curve, or the teardrop yield curves. The use of a plastic potential in conjunction with these yield curves may also prove useful in solving these issues. A detailed analysis of the simulations using the family of Mohr–Coulomb and Teardrop yield curves is beyond the scope of this work and will be presented in a subsequent study. Below, we apply knowledge gained from the simulations presented above, and discuss how alternative yield curves may address deficiencies in the standard VP rheology.

It is possible to include different (non-normal) flow rules with the Mohr–Coulomb family of yield curve. The Mohr–Coulomb yield curve with a pure shear flow rule (Ip et al., 1991) would create fracture angle approximately equal to 45°, independently of the slope of the yield curve. It corresponds to the case $e_G \gg e_F$, hence $\delta \simeq 0$ and $\theta = 45°$, as shown in Fig. 7). This contradicts the Coulomb angle theory, which predicts an angle of fracture that depends solely on the internal angle of friction (Eq. 1). Including an angle of dilatancy with a Mohr–Coulomb yield curve (Tremblay and Mysak, 1997) would allow for different angles of fracture with shear and divergence or convergence along the LKFs depending on δ. Such fracture angle and divergence would be independent of the shear strength and the confining pressure in agreement with Roscoe's angle of fracture. Such a rheology could potentially solve the all four issues. It is also important to note that the Mohr–Coulomb yield curves do not satisfy the convexity requirements of Drucker's postulate of stability. Mohr–Coulomb yield curves in plastic earth mantle models showed different fracture angles corresponding to the Coulomb angle, Roscoe angle, and the intermediate Arthur angles (Buiter et al., 2006; Kaus, 2010; Mancktelow, 2006). However, such geological models are usually incompressible, and making inferences for the compressible formulation of sea ice models is difficult. The investigation of the fracture angles with Mohr–Coulomb yield curves is left for future work.

The Coulombic yield curve uses the two straight limbs from the Mohr–Coulomb yield curve and an elliptical cap of the standard VP rheology for large compressive stresses (Hibler and Schulson, 2000). In this rheology, the flow rule over the two straight limbs is defined by the elliptical yield curve; that is, the ellipse serves as a plastic potential for the Mohr-Coulomb yield curve. The Coulombic yield curve leads to unrealistic and asymmetrical fracture lines *i)* when the stress states lie at the non-differentiable intersection between the straight limbs and the elliptical cap (Ringeisen et al., 2019), and *ii)* when the stress states lie on the two straight limbs with the non-normal flow rule. Note that straight and symmetric fracture lines in this rheology are only possible when all the stress states are located on the Mohr–Coulomb limbs and the flow rule at the fracture line is near-normal, that is, at the location where the normal to the ellipse plastic potential is nearly perpendicular to the limbs of the Mohr–Coulomb yield curve (Ringeisen et al., 2019).

The teardrop yield curve with a normal flow rule (Rothrock, 1975; Zhang and Rothrock, 2005) is divergent for a wide range of normal stresses and for all practical purposes consists of a continuously differentiable version of the Coulombic yield

https://doi.org/10.5194/tc-2020-153
Preprint. Discussion started: 23 June 2020
© Author(s) 2020. CC BY 4.0 License.


curve. This asymmetry between divergent and convergent deformation for different normal stresses decreases the effect of confinement on the fracture angle – issue 2 – and reduces the fracture angle for any confinement pressure – issue 4. This yield curve does not address issue 1, because adding shear strength in the tear-drop yield curve also increases the fracture angle.

The main disadvantage of a non-normal flow rule is the slower numerical convergence. Solving the momentum equation accurately requires more solver iterations and failure to converge is more frequent than for standard normal-flow-rule rheologies. In our simulations, this numerical issue manifests itself by the presence of multiple and asymmetrical fracture lines despite the fact that our experiments are entirely symmetrical. The fracture lines with a normal flow rule are symmetrical and come in pairs (Ringeisen et al., 2019). The poorer numerical convergence in practice will go unnoticed in high-resolution simulations using realistic geometries, since the number of iterations typically used ($O(10)$) is much smaller than that required for full convergence. On the upside, at each time-step, a new iteration typically use the solution from the previous timestep as initial conditions. This, together with slowly varying forcing in space and time, the number of solver iterations per forcing cycle is large, in contrast to the fast changing forcing in this study. Whether this behaviour (asymmetry and multiple fracture lines) will also be present in realistic simulation using spatially and temporally varying wind forcing remains to be tested.

The following criteria should be considered when building a new rheology. The spatial and temporal scaling of sea-ice deformation should agree with observations (Bouchat and Tremblay, 2017; Hutter et al., 2018); the flow rule should reproduce the correct divergence along LKFs (Stern et al., 1995); the yield curve includes some tensile strength (Coon et al., 2007) and reproduces observed distributions of internal stress when ice deforms (Weiss and Schulson, 2009); the distribution of fracture angles should agree with observations (Marko and Thomson, 1977; Erlingsson, 1988; Cunningham et al., 1994; Hutter et al., 2019); the sea ice mechanical strength properties (yield curve) and deformation (flow rule) should vary in time and space depending on the time-varying distribution of the contact normals and floe size distributions, as per observations and laboratory or numerical experiments (Overland et al., 1998; Hutter et al., 2019; Horvat and Tziperman, 2017; Roach et al., 2018; Balendran and Nemat-Nasser, 1993; Dansereau et al., 2016).

Although high spatial resolution observations from satellite are available from optical instruments (e.g., from the Landsat or Sentinel programs), higher temporal resolution of sea ice deformation and flow size distributions are still lacking. So is the combined knowledge of the failure stresses and their associated deformation of sea ice as a 2D granular material. Sea ice floating on the ocean surface can "escape" vertically when ridging under confined compression (Hopkins, 1994). This behaviour differs from laboratory test that use axial symmetry and general knowledge about 3D granular material like sand. Generally, information about sea ice resistance in different configurations (e.g., confinement) and the resulting fracture angles and deformation (ridging or opening) is also still missing, although laboratory scale experimental results are available Weiss et al. (2007); Schulson et al. (2006); Weiss and Schulson (2009). The sea ice flow size distribution varies in time (summer/winter) and space (marginal ice zone/central Arctic) (Rothrock and Thorndike, 1984). These variations change the mechanical properties (e.g., distribution of contact normals) and thermodynamic properties (e.g., lateral melt) of sea ice (Horvat and Tziperman, 2017). Consolidated observations of these two physical processes are needed to design new rheologies for high-resolution climate modelling.

https://doi.org/10.5194/tc-2020-153
Preprint. Discussion started: 23 June 2020
© Author(s) 2020. CC BY 4.0 License.


6 Conclusions

The flow rule, which dictates the post-fracture deformation, has a fundamental effect on the orientation of fractures lines in a viscous-plastic sea ice model. To test this, we added an elliptical plastic potential (allowing for a non-normal flow rule) to the standard viscous plastic rheology with an elliptical yield curve. We tested this new rheology with numerical experiments in uni-axial compression using the standard viscous-plastic model of Hibler (1979). The modeled fracture angles are in agreement with the Roscoe angle, a theory based on experiments with granular materials that includes an angle of dilatancy (Roscoe, 1970; Tremblay and Mysak, 1997). This new rheology partially solves issues raised in an earlier study (Ringeisen et al., 2019). The use of a plastic potential or non-normal flow rule allows for the simulations of smaller fracture angles between pairs of Linear Kinematic Features, in agreement with satellite observations. The fracture angles, however, still depend on the confinement pressure, and the elliptical plastic potential does not modify the direction of deformation at the fracture lines (convergence or divergence), only the ratio of divergence relative to shear. The momentum equations for a rheological model with a non-normal flow rule are more difficult to solve numerically, and produce multiple lines of fractures that are asymmetrical (despite symmetry of the problem), in contrast with a model with a normal flow rule. Understanding the effect of the flow rule on the fracture angle is necessary to design VP rheologies for high-resolution sea-ice modeling that both reproduce fracture angles and deformation along the fracture lines, and the behaviour of sea ice as a granular material.

Designing a rheology for high-resolution simulation requires information on sea ice fracture angles and sea ice strength in a wide range of stress conditions (i.e., compression with or without confinement, pure shear, tension), yet unavailable at high temporal and spatial resolution. The observations of the Multidisciplinary drifting Observatory for the Study of Arctic Climate (MOSAiC, Dethloff et al., 2016) in 2019/2020 may provide valuable data from continuous ice radar imaging, stress sensors, and arrays of drift buoys that will greatly help improve sea ice model dynamics.

Code availability. The modified version of MITgcm used in this study is available at https://github.com/dringeis/MITgcm/tree/ell_nnfr

Author contributions. DR designed the rheology and implemented the code changes with ML. DR ran the experiments. DR and BT designed the theory linking sea ice rheologies and granular matter theory. DR wrote the manuscript with contributions of BT and ML.

Competing interests. The authors declare that they have no conflict of interest.

Acknowledgements. This project was supported by the Deutsche Forschungsgemeinschaft (DFG) through the International Research Training Group "Processes and impacts of climate change in the North Atlantic Ocean and the Canadian Arctic" (IRTG 1904 ArcTrain). This work is a contribution to Natural Sciences and Engineering Research Council Discovery Grant awarded to Tremblay. The authors are thankful to

https://doi.org/10.5194/tc-2020-153
Preprint. Discussion started: 23 June 2020
© Author(s) 2020. CC BY 4.0 License.


425 Mathieu Plante for his comments on this manuscript, and Stephanie Deboeuf and Guillaume Ovarlez for useful discussions on granular materials rheologies.

https://doi.org/10.5194/tc-2020-153
Preprint. Discussion started: 23 June 2020
© Author(s) 2020. CC BY 4.0 License.

References

Aksenov, Y. and Hibler, W. D.: Failure Propagation Effects in an Anisotropic Sea Ice Dynamics Model, in: IUTAM Symposium on Scaling Laws in Ice Mechanics and Ice Dynamics, edited by Dempsey, J. P. and Shen, H. H., Solid Mechanics and Its Applications, pp. 363–372, Springer Netherlands, 2001.

Alshibli, K. A. and Sture, S.: Shear Band Formation in Plane Strain Experiments of Sand, Journal of Geotechnical and Geoenvironmental Engineering, 126, 495–503, https://doi.org/10.1061/(ASCE)1090-0241(2000)126:6(495), https://ascelibrary.org/doi/abs/10.1061/(ASCE)1090-0241(2000)126:6(495), 2000.

Anderson, E. M.: The dynamics of faulting and dyke formation with applications to Britain, Oliver and Boyd, 1942.

Arthur, J. R. F., Dunstan, T., Al-Ani, Q. a. J. L., and Assadi, A.: Plastic deformation and failure in granular media, Géotechnique, 27, 53–74, https://doi.org/10.1680/geot.1977.27.1.53, https://www.icevirtuallibrary.com/doi/abs/10.1680/geot.1977.27.1.53, 1977.

Badgley, F. I.: Heat balance at the surface of the Arctic Ocean, US-IGY Drifting Station Alpha Arctic Ocean 1957-1958, p. 69, http://citeseerx.ist.psu.edu/viewdoc/download?doi=10.1.1.936.1120&rep=rep1&type=pdf#page=71, 1965.

Balendran, B. and Nemat-Nasser, S.: Double sliding model for cyclic deformation of granular materials, including dilatancy effects, Journal of the Mechanics and Physics of Solids, 41, 573–612, https://doi.org/10.1016/0022-5096(93)90049-L, http://www.sciencedirect.com/science/article/pii/002250969390049L, 1993.

Bolton, M. D.: The strength and dilatancy of sands, Géotechnique, 36, 65–78, https://doi.org/10.1680/geot.1986.36.1.65, https://www.icevirtuallibrary.com/doi/abs/10.1680/geot.1986.36.1.65, publisher: ICE Publishing, 1986.

Bouchat, A. and Tremblay, B.: Using sea-ice deformation fields to constrain the mechanical strength parameters of geophysical sea ice, Journal of Geophysical Research: Oceans, pp. n/a–n/a, https://doi.org/10.1002/2017JC013020, http://onlinelibrary.wiley.com/doi/10.1002/2017JC013020/abstract, 2017.

Bouchat, A., Tremblay, L. B., and Hutter, N.: Scaling and statistical properties of sea-ice deformation fields from models participating in the FAMOS Sea-Ice Rheology Experiment, Journal of Geophysical Research: Oceans, In Review, 2020.

Buiter, S. J. H., Babeyko, A. Y., Ellis, S., Gerya, T. V., Kaus, B. J. P., Kellner, A., Schreurs, G., and Yamada, Y.: The numerical sandbox: comparison of model results for a shortening and an extension experiment, Geological Society, London, Special Publications, 253, 29–64, https://doi.org/10.1144/GSL.SP.2006.253.01.02, https://sp.lyellcollection.org/content/253/1/29, publisher: Geological Society of London Section: Analogue and Numerical Sandbox Models, 2006.

Coon, M., Kwok, R., Levy, G., Pruis, M., Schreyer, H., and Sulsky, D.: Arctic Ice Dynamics Joint Experiment (AIDJEX) assumptions revisited and found inadequate, Journal of Geophysical Research: Oceans, 112, C11S90, https://doi.org/10.1029/2005JC003393, http://onlinelibrary.wiley.com/doi/10.1029/2005JC003393/abstract, 2007.

Coon, M. D., Maykut, A., G., Pritchard, R. S., Rothrock, D. A., and Thorndike, A. S.: Modeling The Pack Ice as an Elastic-Plastic Material, AIDJEX BULLETIN, No. 24, 1–106, 1974.

Coulomb, C.: Test on the applications of the rules of maxima and minima to some problems of statics related to architecture, Mem Math Phys, 7, 343–382, 1773.

Cunningham, G., Kwok, R., and Banfield, J.: Ice lead orientation characteristics in the winter Beaufort Sea, in: Proceedings of IGARSS '94 - 1994 IEEE International Geoscience and Remote Sensing Symposium, vol. 3, pp. 1747–1749 vol.3, https://doi.org/10.1109/IGARSS.1994.399553, 1994.

© Author(s) 2020. CC BY 4.0 License.


Dansereau, V., Weiss, J., Saramito, P., and Lattes, P.: A Maxwell elasto-brittle rheology for sea ice modelling, The Cryosphere, 10, 1339–1359, https://doi.org/10.5194/tc-10-1339-2016, http://www.the-cryosphere.net/10/1339/2016/, 2016.

Dethloff, K., Rex, M., and Shupe, M.: Multidisciplinary drifting Observatory for the Study of Arctic Climate (MOSAiC), EGU General Assembly Conference Abstracts, 18, https://ui.adsabs.harvard.edu/#abs/2016EGUGA..18.3064D/abstract, 2016.

Drucker, D. C. and Prager, W.: Soil mechanics and plastic analysis or limit design, Quarterly of applied mathematics, 10, 157–165, 1952.

Dumont, D., Gratton, Y., and Arbetter, T. E.: Modeling the Dynamics of the North Water Polynya Ice Bridge, Journal of Physical Oceanography, 39, 1448–1461, https://doi.org/10.1175/2008JPO3965.1, https://journals.ametsoc.org/doi/abs/10.1175/2008JPO3965.1, 2009.

Erlingsson, B.: Two-dimensional deformation patterns in sea ice, Journal of Glaciology, 34, 301–308, 1988.

Heorton, H. D. B. S., Feltham, D. L., and Tsamados, M.: Stress and deformation characteristics of sea ice in a high-resolution, anisotropic sea ice model, Phil. Trans. R. Soc. A, 376, 20170 349, https://doi.org/10.1098/rsta.2017.0349, http://rsta.royalsocietypublishing.org/content/376/2129/20170349, 2018.

Hibler, W. D.: A viscous sea ice law as a stochastic average of plasticity, Journal of Geophysical Research, 82, 3932–3938, https://doi.org/10.1029/JC082i027p03932, http://onlinelibrary.wiley.com/doi/10.1029/JC082i027p03932/abstract, 1977.

Hibler, W. D.: A Dynamic Thermodynamic Sea Ice Model, Journal of Physical Oceanography, 9, 815–846, https://doi.org/10.1175/1520-0485(1979)009<0815:ADTSIM>2.0.CO;2, http://journals.ametsoc.org/doi/abs/10.1175/1520-0485%281979%29009%3C0815%3AADTSIM%3E2.0.CO%3B2, 1979.

Hibler, W. D. and Schulson, E. M.: On modeling the anisotropic failure and flow of flawed sea ice, Journal of Geophysical Research: Oceans, 105, 17 105–17 120, https://doi.org/10.1029/2000JC900045, http://onlinelibrary.wiley.com/doi/10.1029/2000JC900045/abstract, 2000.

Hopkins, M. A.: On the ridging of intact lead ice, Journal of Geophysical Research: Oceans, 99, 16 351–16 360, https://doi.org/10.1029/94JC00996, http://onlinelibrary.wiley.com/doi/10.1029/94JC00996/abstract, 1994.

Horvat, C. and Tziperman, E.: The evolution of scaling laws in the sea ice floe size distribution, Journal of Geophysical Research: Oceans, pp. n/a–n/a, https://doi.org/10.1002/2016JC012573, http://onlinelibrary.wiley.com/doi/10.1002/2016JC012573/abstract, 2017.

Hutchings, J. K., Heil, P., and Hibler, W. D.: Modeling Linear Kinematic Features in Sea Ice, Monthly Weather Review, 133, 3481–3497, https://doi.org/10.1175/MWR3045.1, http://journals.ametsoc.org/doi/abs/10.1175/MWR3045.1, 2005.

Hutter, N. and Losch, M.: Feature-based comparison of sea ice deformation in lead-permitting sea ice simulations, The Cryosphere, 14, 93–113, https://doi.org/https://doi.org/10.5194/tc-14-93-2020, https://www.the-cryosphere.net/14/93/2020/, 2020.

Hutter, N., Martin, L., and Dimitris, M.: Scaling Properties of Arctic Sea Ice Deformation in a High-Resolution Viscous-Plastic Sea Ice Model and in Satellite Observations, Journal of Geophysical Research: Oceans, 123, 672–687, https://doi.org/10.1002/2017JC013119, https://agupubs.onlinelibrary.wiley.com/doi/abs/10.1002/2017JC013119, 2018.

Hutter, N., Zampieri, L., and Losch, M.: Leads and ridges in Arctic sea ice from RGPS data and a new tracking algorithm, The Cryosphere, 13, 627–645, https://doi.org/https://doi.org/10.5194/tc-13-627-2019, https://www.the-cryosphere.net/13/627/2019/, publisher: Copernicus GmbH, 2019.

Ip, C. F.: Numerical investigation of different rheologies on sea-ice dynamics, Ph.D. thesis, Thesis PhD–Dartmouth College, 1993.

Ip, C. F., Hibler, W. D., and Flato, G. M.: On the effect of rheology on seasonal sea-ice simulations, Annals of Glaciology, 15, 17–25, 1991.

Itkin, P., Losch, M., and Gerdes, R.: Landfast ice affects the stability of the Arctic halocline: Evidence from a numerical model, Journal of Geophysical Research: Oceans, 120, 2622–2635, https://doi.org/10.1002/2014JC010353, https://agupubs.onlinelibrary.wiley.com/doi/abs/10.1002/2014JC010353, _eprint: https://agupubs.onlinelibrary.wiley.com/doi/pdf/10.1002/2014JC010353, 2015.

© Author(s) 2020. CC BY 4.0 License.


Kaus, B. J. P.: Factors that control the angle of shear bands in geodynamic numerical models of brittle deformation, Tectonophysics, 484, 36–47, https://doi.org/10.1016/j.tecto.2009.08.042, http://www.sciencedirect.com/science/article/pii/S0040195109004831, 2010.

Kwok, R.: Deformation of the Arctic Ocean Sea Ice Cover between November 1996 and April 1997: A Qualitative Survey, in: IUTAM Symposium on Scaling Laws in Ice Mechanics and Ice Dynamics, edited by Dempsey, J. P. and Shen, H. H., Solid Mechanics and Its Applications, pp. 315–322, Springer Netherlands, Dordrecht, https://doi.org/10.1007/978-94-015-9735-7, 2001.

König Beatty, C. and Holland, D. M.: Modeling Landfast Sea Ice by Adding Tensile Strength, Journal of Physical Oceanography, 40, 185–198, https://doi.org/10.1175/2009JPO4105.1, http://journals.ametsoc.org/doi/abs/10.1175/2009JPO4105.1, 2010.

Lemieux, J.-F. and Tremblay, B.: Numerical convergence of viscous-plastic sea ice models, Journal of Geophysical Research: Oceans, 114, https://doi.org/10.1029/2008JC005017, https://agupubs.onlinelibrary.wiley.com/doi/abs/10.1029/2008JC005017, 2009.

Losch, M., Menemenlis, D., Campin, J.-M., Heimbach, P., and Hill, C.: On the formulation of sea-ice models. Part 1: Effects of different solver implementations and parameterizations, Ocean Modelling, 33, 129–144, https://doi.org/10.1016/j.ocemod.2009.12.008, https://www.sciencedirect.com/science/article/pii/S1463500309002418, 2010.

Losch, M., Fuchs, A., Lemieux, J.-F., and Vanselow, A.: A parallel Jacobian-free Newton–Krylov solver for a coupled sea ice-ocean model, Journal of Computational Physics, 257, 901–911, https://doi.org/10.1016/j.jcp.2013.09.026, http://www.sciencedirect.com/science/article/pii/S0021999113006402, 2014.

Mancktelow, N. S.: How ductile are ductile shear zones?, Geology, 34, 345–348, https://doi.org/10.1130/G22260.1, https://pubs.geoscienceworld.org/geology/article/34/5/345/129512/How-ductile-are-ductile-shear-zones, publisher: GeoScienceWorld, 2006.

Marko, J. R. and Thomson, R. E.: Rectilinear leads and internal motions in the ice pack of the western Arctic Ocean, Journal of Geophysical Research, 82, 979–987, https://doi.org/10.1029/JC082i006p00979, https://agupubs.onlinelibrary.wiley.com/doi/10.1029/JC082i006p00979, 1977.

Mohr, O.: Welche Umstände bedingen die Elastizitätsgrenze und den Bruch eines Materials, Zeitschrift des Vereins Deutscher Ingenieure, 46, 1572–1577, 1900.

Nguyen, A. T., Menemenlis, D., and Kwok, R.: Arctic ice-ocean simulation with optimized model parameters: Approach and assessment, Journal of Geophysical Research: Oceans, 116, C04 025, https://doi.org/10.1029/2010JC006573, http://onlinelibrary.wiley.com/doi/10.1029/2010JC006573/abstract, 2011.

Nguyen, A. T., Kwok, R., and Menemenlis, D.: Source and Pathway of the Western Arctic Upper Halocline in a Data-Constrained Coupled Ocean and Sea Ice Model, Journal of Physical Oceanography, 42, 802–823, https://doi.org/10.1175/JPO-D-11-040.1, https://journals.ametsoc.org/doi/full/10.1175/JPO-D-11-040.1, publisher: American Meteorological Society, 2012.

Overland, J. E., McNutt, S. L., Salo, S., Groves, J., and Li, S.: Arctic sea ice as a granular plastic, Journal of geophysical research, 103, 21 845–21 868, https://www.researchgate.net/profile/James_Overland/publication/240487097_Arctic_sea_ice_as_a_granular_plastic/links/55cb6a2c08aeb975674c796b.pdf, 1998.

Rampal, P., Bouillon, S., Ólason, E., and Morlighem, M.: neXtSIM: a new Lagrangian sea ice model, The Cryosphere, 10, 1055–1073, https://doi.org/10.5194/tc-10-1055-2016, http://www.the-cryosphere.net/10/1055/2016/, 2016.

Ringeisen, D., Losch, M., Tremblay, L. B., and Hutter, N.: Simulating intersection angles between conjugate faults in sea ice with different viscous–plastic rheologies, The Cryosphere, 13, 1167–1186, https://doi.org/https://doi.org/10.5194/tc-13-1167-2019, https://www.the-cryosphere.net/13/1167/2019/, 2019.

https://doi.org/10.5194/tc-2020-153
Preprint. Discussion started: 23 June 2020
© Author(s) 2020. CC BY 4.0 License.

Roach, L. A., Horvat, C., Dean, S. M., and Bitz, C. M.: An Emergent Sea Ice Floe Size Distribution in a Global Coupled Ocean-Sea Ice Model, Journal of Geophysical Research: Oceans, 123, 4322–4337, https://doi.org/10.1029/2017JC013692, https://agupubs.onlinelibrary.wiley.com/doi/abs/10.1029/2017JC013692, _eprint: https://agupubs.onlinelibrary.wiley.com/doi/pdf/10.1029/2017JC013692, 2018.

Roscoe, K. H.: The Influence of Strains in Soil Mechanics, Géotechnique, 20, 129–170, https://doi.org/10.1680/geot.1970.20.2.129, https://www.icevirtuallibrary.com/doi/abs/10.1680/geot.1970.20.2.129, 1970.

Rothrock, D. A.: The energetics of the plastic deformation of pack ice by ridging, Journal of Geophysical Research, 80, 4514–4519, https://doi.org/10.1029/JC080i033p04514, http://onlinelibrary.wiley.com/doi/10.1029/JC080i033p04514/abstract, 1975.

Rothrock, D. A. and Thorndike, A. S.: Measuring the sea ice floe size distribution, Journal of Geophysical Research: Oceans, 89, 6477–6486, https://doi.org/10.1029/JC089iC04p06477, http://onlinelibrary.wiley.com/doi/10.1029/JC089iC04p06477/abstract, 1984.

Schulson, E. M. and Hibler, W. D.: Fracture of the winter sea ice cover on the Arctic ocean, Comptes Rendus Physique, 5, 753–767, https://doi.org/10.1016/j.crhy.2004.06.001, http://www.sciencedirect.com/science/article/pii/S1631070504001318, 2004.

Schulson, E. M., Fortt, A. L., Iliescu, D., and Renshaw, C. E.: On the role of frictional sliding in the compressive fracture of ice and granite: Terminal vs. post-terminal failure, Acta Materialia, 54, 3923–3932, https://doi.org/10.1016/j.actamat.2006.04.024, http://www.sciencedirect.com/science/article/pii/S1359645406003120, 2006.

Spreen, G., Kwok, R., Menemenlis, D., and Nguyen, A. T.: Sea-ice deformation in a coupled ocean–sea-ice model and in satellite remote sensing data, The Cryosphere, 11, 1553–1573, https://doi.org/10.5194/tc-11-1553-2017, https://www.the-cryosphere.net/11/1553/2017/, 2017.

Stern, H. L., Rothrock, D. A., and Kwok, R.: Open water production in Arctic sea ice: Satellite measurements and model parameterizations, Journal of Geophysical Research: Oceans, 100, 20 601–20 612, https://doi.org/10.1029/95JC02306, https://agupubs.onlinelibrary.wiley.com/doi/abs/10.1029/95JC02306, publisher: John Wiley & Sons, Ltd, 1995.

Stroeve, J., Barrett, A., Serreze, M., and Schweiger, A.: Using records from submarine, aircraft and satellites to evaluate climate model simulations of Arctic sea ice thickness, The Cryosphere, 8, 1839–1854, https://doi.org/10.5194/tc-8-1839-2014, http://www.the-cryosphere.net/8/1839/2014/, 2014.

Tremblay, L.-B. and Mysak, L. A.: Modeling Sea Ice as a Granular Material, Including the Dilatancy Effect, Journal of Physical Oceanography, 27, 2342–2360, https://doi.org/10.1175/1520-0485(1997)027<2342:MSIAAG>2.0.CO;2, http://journals.ametsoc.org/doi/abs/10.1175/1520-0485(1997)027%3C2342:MSIAAG%3E2.0.CO;2, 1997.

Vardoulakis, I.: Shear band inclination and shear modulus of sand in biaxial tests, International Journal for Numerical and Analytical Methods in Geomechanics, 4, 103–119, https://doi.org/10.1002/nag.1610040202, https://onlinelibrary.wiley.com/doi/abs/10.1002/nag.1610040202, 1980.

Vardoulakis, I. and Graf, B.: Calibration of constitutive models for granular materials using data from biaxial experiments, Géotechnique, 35, 299–317, https://doi.org/10.1680/geot.1985.35.3.299, https://www.icevirtuallibrary.com/doi/abs/10.1680/geot.1985.35.3.299, publisher: ICE Publishing, 1985.

Vermeer, P. A.: The orientation of shear bands in biaxial tests, Géotechnique, https://doi.org/10.1680/geot.1990.40.2.223, https://www.icevirtuallibrary.com/doi/abs/10.1680/geot.1990.40.2.223, 1990.

Vermeer, P. A. and De Borst, R.: Non-associated plasticity for soils, concrete and rock, HERON, 29 (3), 1984, 1984.

Wang, K.: Observing the yield curve of compacted pack ice, Journal of Geophysical Research: Oceans, 112, C05 015, https://doi.org/10.1029/2006JC003610, http://onlinelibrary.wiley.com/doi/10.1029/2006JC003610/abstract, 2007.

https://doi.org/10.5194/tc-2020-153
Preprint. Discussion started: 23 June 2020
© Author(s) 2020. CC BY 4.0 License.


Weiss, J. and Schulson, E. M.: Coulombic faulting from the grain scale to the geophysical scale: lessons from ice, Journal of Physics D: Applied Physics, 42, 214 017, https://doi.org/10.1088/0022-3727/42/21/214017, http://stacks.iop.org/0022-3727/42/i=21/a=214017, 2009.

Weiss, J., Schulson, E. M., and Stern, H. L.: Sea ice rheology from in-situ, satellite and laboratory observations: Fracture and friction, Earth and Planetary Science Letters, 255, 1–8, https://doi.org/10.1016/j.epsl.2006.11.033, http://www.sciencedirect.com/science/article/pii/S0012821X06008430, 2007.

Wilchinsky, A. V. and Feltham, D. L.: Modelling the rheology of sea ice as a collection of diamond-shaped floes, Journal of Non-Newtonian Fluid Mechanics, 138, 22–32, https://doi.org/10.1016/j.jnnfm.2006.05.001, http://www.sciencedirect.com/science/article/pii/S0377025706001029, 2006.

Wilchinsky, A. V., Feltham, D. L., and Hopkins, M. A.: Effect of shear rupture on aggregate scale formation in sea ice, Journal of Geophysical Research: Oceans, 115, C10 002, https://doi.org/10.1029/2009JC006043, http://onlinelibrary.wiley.com/doi/10.1029/2009JC006043/abstract, 2010.

Williams, J., Tremblay, L. B., and Lemieux, J.-F.: The effects of plastic waves on the numerical convergence of the viscous–plastic and elastic–viscous–plastic sea-ice models, Journal of Computational Physics, 340, 519–533, https://doi.org/10.1016/j.jcp.2017.03.048, http://www.sciencedirect.com/science/article/pii/S0021999117302498, 2017.

Zhang, J. and Hibler, W. D.: On an efficient numerical method for modeling sea ice dynamics, Journal of Geophysical Research: Oceans, 102, 8691–8702, https://doi.org/10.1029/96JC03744, http://onlinelibrary.wiley.com/doi/10.1029/96JC03744/abstract, 1997.

Zhang, J. and Rothrock, D. A.: Effect of sea ice rheology in numerical investigations of climate, Journal of Geophysical Research: Oceans, 110, C08 014, https://doi.org/10.1029/2004JC002599, http://onlinelibrary.wiley.com/doi/10.1029/2004JC002599/abstract, 2005.